

PAPER • OPEN ACCESS

Complex band structure with non-orthogonal basis set: analytical properties and implementation in the SIESTA code

To cite this article: E Bosoni and S Sanvito 2022 *J. Phys.: Condens. Matter* **34** 105501

View the [article online](#) for updates and enhancements.

You may also like

- [Numerical study of systems with diagonal and off-diagonal disorder in a non-orthogonal basis](#)
N V Cohan and M Weissmann
- [Bi-orthogonal mutually unbiased bases for N-qubit systems](#)
Juan J Díaz, Isabel Sainz and Andrei B Klimov
- [Wave-particle duality employing quantum coherence in superposition with non-orthogonal pointers](#)
Sreetama Das, Chiranjib Mukhopadhyay, Sudipto Singha Roy et al.



IOP | ebooks™

Bringing together innovative digital publishing with leading authors from the global scientific community.

Start exploring the collection—download the first chapter of every title for free.

Complex band structure with non-orthogonal basis set: analytical properties and implementation in the SIESTA code

E Bosoni*  and S Sanvito 

School of Physics and CRANN, Trinity College, College Green, Dublin 2, Ireland

E-mail: bosonie@tcd.it

Received 27 August 2021, revised 22 November 2021

Accepted for publication 8 December 2021

Published 23 December 2021



Abstract

The complex band structure (CBS), although not directly observable, determines many properties of a material where the periodicity is broken, such as surfaces, interfaces and defects. Furthermore, its knowledge helps in the interpretation of electronic transport calculations and in the study of topological materials. Here we extend the transfer matrix method, often used to compute the complex bands, to electronic structures constructed using an atomic non-orthogonal basis set. We demonstrate that when the overlap matrix is not the identity, the non-orthogonal case, spurious features appear in the analytic continuation of the band structure to the complex plane. The properties of these are studied both numerically and analytically and discussed in the context of existing literature. Finally, a numerical implementation to extract the CBS from periodic calculations carried out with the density functional theory code SIESTA is presented. This is constructed as a simple post-processing tool, and it is therefore amenable to high-throughput studies of insulators and semiconductors.

Keywords: complex band structure, non-orthogonal basis sets, density functional theory

(Some figures may appear in colour only in the online journal)

1. Introduction

One of the central quantities when studying the electronic structure of a crystal is the dispersion relation, $E(\mathbf{k})$, between the energy, E , and the crystal momentum, \mathbf{k} , a property obtained by solving the time-independent Schrödinger equation for a periodic system. The concept is rather general and can be extended to other problems associated to a periodic potential, such as the determination of the modes of an electromagnetic field in dielectric crystals [1, 2].


When E and \mathbf{k} are real quantities, the $E(\mathbf{k})$ relation is known as the band structure. In this situation for every real energy E , the allowed real wave-vectors \mathbf{k} (if any) describe the propagating states of the crystal, whose wave function has a mathematical expression following Bloch's theorem,

$$\psi_{\mathbf{k}}(\mathbf{r}) = e^{i\mathbf{k}\mathbf{r}} u_{\mathbf{k}}(\mathbf{r}), \quad (1)$$

where $u_{\mathbf{k}}(\mathbf{r})$ is a function with the same periodicity of the potential.

The wave vector \mathbf{k} needs to be real in order to ensure that the wave functions remain finite over the entire space, but this is not a requirement of the Schrödinger equation itself. It is then possible to generalize the dispersion relation $E(\mathbf{k})$ to complex wave vectors. In such case, the wave function, $\psi_{\mathbf{k}}(\mathbf{r})$, of type (1) represents an evanescent state that grows or decays exponentially from one unit cell to the next. Although such

* Author to whom any correspondence should be addressed.

 Original content from this work may be used under the terms of the [Creative Commons Attribution 4.0 licence](https://creativecommons.org/licenses/by/4.0/). Any further distribution of this work must maintain attribution to the author(s) and the title of the work, journal citation and DOI.

evanescent states are forbidden by the translational symmetry, namely they violate Bloch's theorem, they become important when the periodicity is broken, for example, at a surface or an interface.

When one allows \mathbf{k} to be complex, $E(\mathbf{k})$ becomes a multi-valued $\mathbb{C} \mapsto \mathbb{C}$ function that can be studied with the tools of complex analysis, giving an entirely new perspective to the understanding of the electronic structure of a crystal. The analytical properties of $E(\mathbf{k})$ were first derived by Kohn [3] for strictly 1D situations and then extended by Heine [4] and Prodan [5] to 2D and 3D, where \mathbf{k} is allowed to be complex in one direction only. This is the most interesting situation as it effectively includes 1D materials, but also 2D/3D ones with a surface, where the components of \mathbf{k} parallel to the surface remain good quantum numbers (real) and can be treated as parameters [6, 7].

Even though the study of the complex $E(\mathbf{k})$ relation is of interest in its entirety, only energies with $\Im m(E) = 0$ hold a physical meaning. The set of real energies associated to a complex \mathbf{k} is what is generally called the complex band structure (CBS). Heine showed in a pioneering study [4] that the CBS can be viewed as a collection of 'line of real energies' with well defined behaviors in the complex plane. Kreigher then revised all the properties of the complex $E(\mathbf{k})$ dispersion and of the 'lines of real energy' in the case of finite-band models, where the electronic wave functions are expanded over a finite basis set [8]. In this case only algebraic arguments (no complex analysis) can be used to derive the analytical properties of $E(\mathbf{k})$. However, a fundamental assumption of Kreigher's theory is that the basis set is orthonormal. To the best of our knowledge, to date there is no generalization to the non-orthogonal case, despite the fact that non-orthogonal basis sets are often used in electronic structure theory and in the calculation of the CBS [9]. Notably in literature there are many examples of computational techniques and CBS calculations for real materials, but only recently effort has been dedicated in providing a comprehensive and unified perspective to the study of the CBS [10].

The goal of our paper is twofold. Firstly, we introduce a simple scheme, based on the transfer matrix technique, for the calculation of the CBS (section 2). This is implemented as a general post-processing tool for the density functional theory (DFT) code SIESTA [11, 12], which uses a local atom-centered non-orthogonal basis set. Our results pose some questions related to the properties of the CBS in the presence of overlapping basis functions, whose analysis, both analytical and numerical, constitutes the second part of our work (sections 3–5). As such, our work can also be viewed as a practical guide to interpret the results of CBS calculations in presence of a non-orthogonal basis set.

2. CBS calculation: theory and implementation

As in Reuter's topical review [10] we consider here the situation in which only one component of the wave vector, \mathbf{k} , is complex. As a matter of notation such complex component is denoted with k , while the remaining real space will be described by the vector \mathbf{k}_{\parallel} (in either 1D or 2D depending on

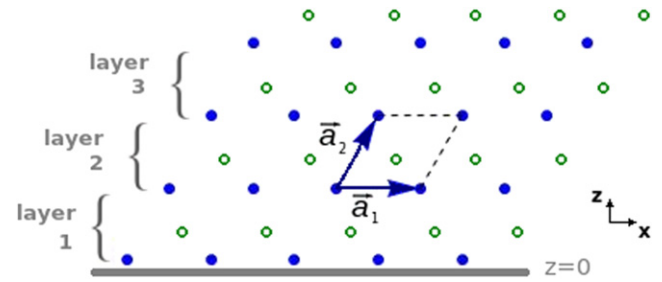


Figure 1. Schematic representation of the layered structure for 2D BN. The $z = 0$ defines the plane where the translational symmetry is broken, so that the complex wave vector is associated to the z direction. The crystal is then periodic in the x direction with lattice vector \vec{a}_1 (\vec{a}_1 and \vec{a}_2 are the primitive lattice vector for monolayer BN). Color code: B blue circles, N green circles.

the dimensionality of the crystal). Hence, we are describing the situation in which the periodicity of the crystal is maintained only in the plane spanned by \mathbf{k}_{\parallel} . The first step in the calculation of the CBS of a crystal consists in defining the desired layered structure and in writing the system Hamiltonian accordingly [13, 14]. An example of this procedure is provided in figure 1. Here a 2D BN crystal is cut across a B-atom plane, defined by $z = 0$, so that the periodicity is lost in the z direction, while the crystal remains periodic with lattice vector \vec{a}_1 in the orthogonal x direction. A cell must then be constructed that allows to create layers perpendicular to the z direction. A layer is defined by grouping some repetitions of the chosen cell. In our example we choose the unit cell of BN since it already meets the requirement to form layers perpendicular to z . Importantly, it is not necessary that the layer itself repeats periodically in the z direction. Instead, it is sufficient that the chosen cell can be used to replicate the entire crystal should the $z = 0$ surface not to exist and a subset of the repeated cells can be grouped to constitute a layer in z direction. With this choice, the complex component of the wave vector is associated to the z direction.

Let us now assume that the wave function and all the operators are expanded over an atomic-like basis set. If the matrix elements are arranged according to the layered structure defined before, the Hamiltonian will have the following generic block form,

$$\bar{H}_L = \begin{bmatrix} H_{11} & H_{12} & H_{13} & H_{14} & \dots \\ H_{21} & H_{22} & H_{23} & H_{24} & \dots \\ H_{31} & H_{32} & H_{33} & H_{34} & \dots \\ H_{41} & H_{42} & H_{43} & H_{44} & \dots \\ \dots & \dots & \dots & \dots & \dots \end{bmatrix}, \quad (2)$$

where the matrix H_{ij} contains all the matrix elements that couple layer i with layer j . Thus, the Hermitian matrix H_{ii} describes all the interactions with the i th layer and $i = 1$ corresponds to the surface layer. If one neglects any alteration of the electronic structure due to the presence of the surface (e.g. screening, geometrical relaxation, etc), namely if the electronic structure is defined by a truncated version of the bulk Hamiltonian, then we have $H_{ii} = H_D$ for all the i layers, meaning that the matrices that describe the interaction within a layer are identical for every layer. This is also the case for the

matrix describing the interaction of a layer at the position i with the layer at the position $i + n$, which we define as H_n . Note that the finite range of the interaction establishes that eventually H_n must vanish for a sufficiently large n . The complete Hamiltonian can then be written as

$$\bar{H}_L = \begin{bmatrix} H_D & H_1^\dagger & H_2^\dagger & H_3^\dagger & \dots \\ H_1 & H_D & H_1^\dagger & H_2^\dagger & \dots \\ H_2 & H_1 & H_D & H_1^\dagger & \dots \\ H_3 & H_2 & H_1 & H_D & \dots \\ \dots & \dots & \dots & \dots & \dots \end{bmatrix}. \quad (3)$$

A Hamiltonian of the form (3) can always be written, once a local basis set is chosen. This is the case, for instance, of tight-binding models [13] and many local-orbital DFT codes. In our implementation we extract such matrix elements from the DFT SIESTA package, which utilises a numerical multiple-zetas atom-centered local-orbital basis [11]. One has then to assume that a SIESTA calculation for the bulk has been performed, so that the fully converged Kohn–Sham Hamiltonian is available. Since no self-consistent calculations are further required, the problem at this point is completely equivalent to a tight-binding one. However, at variance with many conventional tight-binding methods, the supplementary complication of using SIESTA is that the basis is strictly non-orthogonal. Importantly, with the same general argument used for the Hamiltonian, one can easily realise that also the overlap matrix, \bar{S}_L , can be written in the block form (3), where now the matrices S_D and S_n contain the overlap matrix elements within the layer and between layers i and $i + n$, respectively. Note that the range of the overlap matrix is in general shorter than that of the Hamiltonian, so that S_n may vanish for an n smaller than the one needed by \bar{H}_L .

Since the periodicity is preserved in the plane orthogonal to the z direction, \mathbf{k}_\parallel remains a good quantum number. Bloch's theorem can be applied so that, in principle, the infinitely dimensional Hamiltonian \bar{H}_L can be replaced by a set of \mathbf{k}_\parallel -dependent Hamiltonians, $\bar{H}_L^{\mathbf{k}_\parallel}$, where now the submatrices H_D , S_D , H_n and S_n are \mathbf{k}_\parallel -dependent and $N \times N$ dimensional, with N being the number of basis functions describing the in-plane unit cell (these are now denoted as $H_D^{\mathbf{k}_\parallel}$, $S_D^{\mathbf{k}_\parallel}$, $H_n^{\mathbf{k}_\parallel}$ and $S_n^{\mathbf{k}_\parallel}$). In what follows we always assume to solve such \mathbf{k}_\parallel -dependent problem for some value of \mathbf{k}_\parallel . The corresponding Schrödinger equation simply writes (for the ease of notation we drop the \mathbf{k}_\parallel superscript),

$$\bar{H}_L \Psi = E \bar{S}_L \Psi, \quad (4)$$

where the wave function Ψ is a column vector $(\varphi_1, \varphi_2, \dots, \varphi_n, \dots)^T$, with φ_i being the N -dimensional vector describing the i th layer.

In conventional band-structure theory one has to find all real energies corresponding to a given set of wave vectors, $(k, \mathbf{k}_\parallel)$, where also k is real. Here we want to achieve the opposite, namely to compute all real and complex values of k corresponding to a given \mathbf{k}_\parallel and a given real energy, E . In principle one can still use equation (4) together with a root-tracking algorithm and look for the real energies associated to k . This, however, is expected to be highly inefficient since now k spans

the large $\mathbb{C} = \mathbb{R} \times \mathbb{R}$ space. Then, there are two main strategies to compute the $(k, \mathbf{k}_\parallel) \rightarrow E$ relation, by using either the wave function (transfer matrix technique) or the Green's function [10]. Here we follow the first approach by extending the strategy proposed in reference [13] to interaction extending beyond the nearest-neighbour layer [10] and to non-orthogonal basis sets.

The idea is to associate the Hamiltonian \bar{H}_L to an infinite periodic system and write the wave function Ψ in its Bloch form, $\Psi = \frac{1}{\sqrt{N}} \sum_l e^{ikal} \varphi_l$, where a is the separation between two adjacent layers. The block-diagonal structure of the Hamiltonian \bar{H}_L and of the overlap matrix \bar{S}_L is such that the Schrödinger equation becomes

$$\begin{aligned} H_D \varphi_i + \sum_{n=1}^{\infty} (e^{inka} H_n \varphi_{i+n} + e^{-inka} H_n^\dagger \varphi_{i-n}) \\ = E S_D \varphi_i + E \sum_{n=1}^{\infty} (e^{inka} S_n \varphi_{i+n} + e^{-inka} S_n^\dagger \varphi_{i-n}). \end{aligned} \quad (5)$$

In practice the sums in (5) are finite, since the range of the Hamiltonian and the overlap matrix is finite, namely H_n and S_n are zero matrices for sufficiently large n 's. Then, (5) can be combined with a series of tautologies $\varphi_i = \varphi_i$ and Bloch relations $\varphi_{i+1} = e^{ika} \varphi_i$ to give an associated generalized eigenvalue equation, whose eigenvalues are e^{ika} . Assuming that the interaction extends only to the second layer ($H_n = 0$, $S_n = 0$ for $n > 2$) this explicitly writes

$$\begin{aligned} e^{ika} \begin{bmatrix} D_2^\dagger & D_1^\dagger & 0 & 0 \\ 0 & I & 0 & 0 \\ 0 & 0 & I & 0 \\ 0 & 0 & 0 & I \end{bmatrix} \begin{bmatrix} \varphi_{i+1} \\ \varphi_i \\ \varphi_{i-1} \\ \varphi_{i-2} \end{bmatrix} \\ = \begin{bmatrix} 0 & -D_D & -D_1 & -D_2 \\ I & 0 & 0 & 0 \\ 0 & I & 0 & 0 \\ 0 & 0 & I & 0 \end{bmatrix} \begin{bmatrix} \varphi_{i+1} \\ \varphi_i \\ \varphi_{i-1} \\ \varphi_{i-2} \end{bmatrix}, \end{aligned} \quad (6)$$

where $D_n = H_n - E S_n$. Equation (6) now can be solved for real energies E to give the allowed k values (both real and imaginary).

In general the equation (6) can be solved by inverting the matrix on the left-hand side and then by solving a standard eigenvalue problem. However, such matrix is often singular and alternative numerical strategies need to be designed to remedy the problem [9, 10]. The simplest approach is to avoid the matrix inversion and to solve a generalized eigenvalue problem, instead. This is the strategy we adopt in our implementation. A generalized eigenvalue problem is more sophisticated than the standard one, since it allows zero and infinite eigenvalues. Furthermore, in the situation of near-to-singular matrices, solving the generalized eigenvalue might yield numerical instabilities by generating large eigenvalues, hence large k 's. In practice we have rarely encountered this problem and furthermore, the most relevant states (for instance to transport) are those with small imaginary k , which are associated to slowly decaying states. A second drawback of the implemented method is that one needs to handle $(N \cdot N_R) \times$

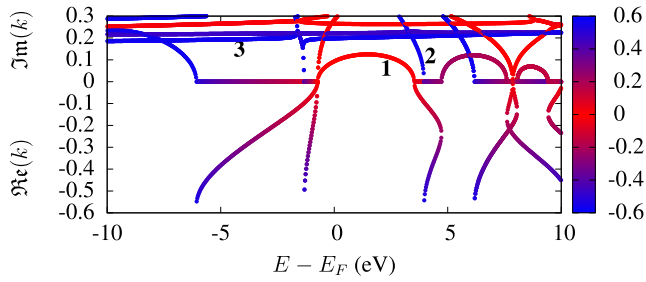


Figure 2. CBS of MgS along the [111] direction at $\mathbf{k}_{\parallel} = (0, 0)$ obtained with our method. The crystal structure is extracted from the ICSD [19] database (identifier Mg1S1_ICSD_53939). The SIESTA calculation employs a double-zeta plus polarization basis set and a k -grid cutoff of 30 Å. The vertical axis is divided into two regions. Pure real bands ($\Re(k)$, obtained when $\Im(k) = 0$) are reported below the origin (this is the standard band structure). Imaginary bands are shown above the origin. The colors encode the real component of the wave-vector, $\Re(k)$ (pure imaginary bands have $\Re(k) = 0$). The units of k are 1/Bohr.

($N \cdot N_R$) dimensional matrices, where N is the number of orbital in the unit cell of the layer (the dimension of H_D , H_n , etc.) and N_R is the range of the interaction (the number of layers a given layer interacts with). This, however, is not a major issue, since in highly converged SIESTA calculations N is usually relatively small (as a rule of thumb one has to consider of the order of 20 basis functions per atom). Furthermore, N_R is regulated by the range of the interaction, which in turn can be tuned in SIESTA by an appropriate choice of the radial cutoff of the basis functions. In our experience for well-converged calculations we have always found $N_R < 5$.

Concerning the practical implementation of our method within SIESTA [11, 12], the Hamiltonian and overlap matrix are extracted from the .HSX file, while the basis set is contained in the ORBI_NDX one. Crystal structure information is stored in the .xv file, which is also extracted. Note that these are all output of a self-consistent calculation. The generalized eigenvalue problem of equation (6) is solved with the ZGGEV routine of the LAPACK library [15]. There are no restrictions to the shape of the cell to compute and the CBS can be extracted along any of the three directions perpendicular to the planes formed by the three lattice vectors. Tools for managing the crystal lattice (PYMATGEN [16] and ASE [17], for instance) can be used to set a minimal cell exposing a particular surface and allow us to explore the CBS in any possible direction. The entire algorithm is implemented in FORTRAN and it is publicly available [18].

An example of CBS computed with our method is reported in figure 2. This is for MgS, a cubic crystal with rock-salt structure (space group $Fm\bar{3}m$, # 225), and calculated along the [111] direction at $\mathbf{k}_{\parallel} = (0, 0)$. In the plot the energy goes on the horizontal axis, while the k vector is on the vertical one. The negative side of the vertical axis reports $\Re(k)$ for states having $\Im(k) = 0$, namely the conventional band structure. In contrast the positive side contains $\Im(k)$ for complex k , namely it is the extension of the band structure to the complex plane. The bands are also color coded according to the magnitude of $\Re(k)$ (this information is redundant in the case of real k).

Three different kinds of complex bands can be identified in figure 2. The first type (type-1) consists of semicircular

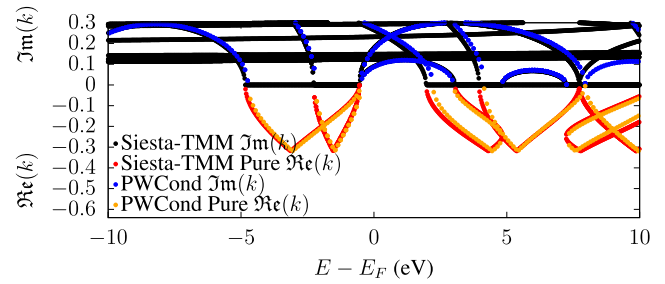


Figure 3. CBS of MgS along the [100] direction at $\mathbf{k}_{\parallel} = (0, 0)$. Here we compare results obtained with our method with those computed using the plane-wave code PWCOND. The SIESTA basis and cutoff are the same as those reported in figure 2. The plane-wave DFT calculation has been performed with plane-wave cutoff of 100 Ry. Pure real bands are reported below the origin, while imaginary ones are above. In the legends TMM means transfer matrix method (the one described here).

bands, which connect two points with $\Im(k) = 0$ (two points on the real plane). An example of these is the low-lying red band connecting the edges of the MgS bandgap, between the energies $E \sim -0.6$ eV and $E \sim 4$ eV (energies are measured with respect to the Fermi energy, E_F). Instead, type-2 bands are those originating from a point on the real plane and growing toward $\Im(k) = \infty$. These can have rather severe curvature and one example is provided by the blue band reconnecting to the $\Im(k) = 0$ plane just above the bandgap ($E \sim 4.3$ eV). Finally our calculation reveals the presence of flat bands (type-3), characterized by an almost constant $\Im(k)$ value over the entire energy range. These are well evident in the region at $\Im(k) > 0.2$ Bohr $^{-1}$. While the behavior of the first two types of bands is consistent with the analytic properties of the CBS (see next section), the flat bands are not expected.

In order to validate our method we perform additional CBS calculations with the PWCOND package [20]. This implements Landauer theory for electronic transport within the plane-wave DFT code QUANTUM ESPRESSO [21]. In this case the CBS is obtained with the Green's function formalism [20] and, most importantly, with an electronic structure expanded over an orthogonal basis set (plane-waves). Such comparison is presented in figure 3 again for MgS, but this time along the [100] direction at $\mathbf{k}_{\parallel} = (0, 0)$. We have changed the direction of the CBS from that of figure 2, since PWCOND can support calculations only for monoclinic cells and the [100] direction allows us to use a monoclinic cell containing only four atoms. When comparing results we ensure that the two DFT calculations are performed at the same level of convergence. As expected, the real bands match closely, with the small differences being related to the use of different pseudopotentials and to the various details of the two codes. Such good agreement is also found for the complex bands of type 1 and 2, namely for the complex bands with at least one connection to the real plane. In contrast the flat bands (type-3) appear to be a feature unique of our SIESTA implementation and are not present in the PWCOND results. This suggests that type-3 bands may be associated to the quality of the basis set.

Such hypothesis can be tested by computing the CBS with our implementation and slightly different choices of basis set.

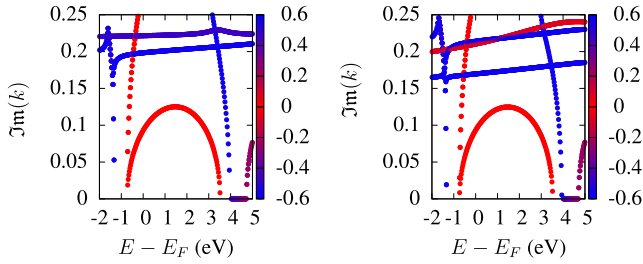


Figure 4. CBS of MgS along the [111] direction at $\mathbf{k}_{\parallel} = (0, 0)$. The SIESTA calculation employs a double-zeta plus polarization basis set and a k -grid cutoff of 30 Å. The bands shown on the (right-hand side panel) are obtained with a basis set having the cutoff radius for the Mg orbitals 10% larger than those used for the bands shown in the (left-hand side panel). The colors encode the real component of the wave-vector, $\Re(k)$. The units of k are 1/Bohr.

This is done in figure 4 again for MgS along the [111] direction at $\mathbf{k}_{\parallel} = (0, 0)$, where we compare the original complex bands of figure 2 (left panel) with those obtained by increasing the cutoff radius of the Mg orbitals by 10% (right panel). Clearly, by looking at figure 4, although type-1 and type-2 bands are almost identical (compare the left- and right-hand panel), the flat type-3 bands change significantly. In fact, their $\Im(k)$ values reduce substantially as the cutoff radius is increased. This calls for a thorough review of the analytical properties of the CBS, in order to gain more insight on the origin of the type-3 bands.

3. Analytical properties of the complex band structure

Taking from the work of Kohn [3] and Heine [4], here we review the analytical properties of the complex dispersion relation, $E(\mathbf{k})$, and of the ‘lines of real energy’. For most of the proofs we follow Krieger’s work on finite-band models [8], unless otherwise specified. In the Schrödinger equation for a periodic system,

$$\hat{H}\psi_{\mathbf{k}}(\mathbf{r}) = E\psi_{\mathbf{k}}(\mathbf{r}), \quad (7)$$

the Hamiltonian, \hat{H} , acts on the generic Bloch’s state,

$$\psi_{\mathbf{k}}(\mathbf{r}) = e^{i\mathbf{k}\mathbf{r}}u_{\mathbf{k}}(\mathbf{r}), \quad (8)$$

where $u_{\mathbf{k}}$ is a function with the same periodicity of the potential that satisfies

$$\hat{H}(\mathbf{k})u_{\mathbf{k}}(\mathbf{r}) = Eu_{\mathbf{k}}(\mathbf{r}), \quad \hat{H}(\mathbf{k}) = e^{-i\mathbf{k}\mathbf{r}}\hat{H}e^{i\mathbf{k}\mathbf{r}}. \quad (9)$$

From equation (9) one can show that $\hat{H}(\mathbf{k})$ is always a polynomial function of the components of \mathbf{k} , even in the presence of spin-orbit interaction. If now one expands $u_{\mathbf{k}}(\mathbf{r})$ over a set of basis functions, $\phi_l(\mathbf{r})$, (for the moment orthogonal)

$$u_{\mathbf{k}}(\mathbf{r}) = \sum_l c_l \phi_l(\mathbf{r}), \quad (10)$$

the Schrödinger equation will translate into a matrix equation for the coefficients, c_l ’s,

$$\bar{\bar{H}}(\mathbf{k})\mathbf{c} = E\mathbf{c}, \quad (11)$$

where all the matrix elements of $\bar{\bar{H}}(\mathbf{k})$ are still polynomial functions of the components of \mathbf{k} .

We now allow one component of \mathbf{k} to be complex, while the other two remain real. If $\bar{\bar{H}}(\mathbf{k})$ is an $N \times N$ matrix, then there will be N solutions of equation (11), $E_i(\mathbf{k})$, which form the full complex dispersion relation. In complex analysis $E_i(\mathbf{k})$ can be seen as the Riemann surfaces of the complex multi-valued function, $E(\mathbf{k})$. With this in mind, a number of analytical properties of $E(\mathbf{k})$ can be demonstrated.

- (a) The eigenvalues $E_i(\mathbf{k})$ are analytic functions of \mathbf{k} except at a set of isolated singular points corresponding to the branch points of $E(\mathbf{k})$. At a branch point two Riemann surfaces connect on the complex plane. To be more formal we can use Needham’s operative definition [22]. A point q will be a branch point, if for any close loop in k -space around it, it is not possible to return to the same $E(k)$. For a generic q , if one starts from a point \bar{k} corresponding to $E(\bar{k})$, once a loop around q is concluded, the energy is still $E(\bar{k})$. However, if q is a branch point the statement is not true. We know that $E(k)$ is a multi-valued complex function. Therefore, by looping around a branch point we end up to another value of $E(k)$ for the same k . In the discussion we have dropped the vector symbol for \mathbf{k} , since we are focusing on the complex component only. Thus, in general q depends on \mathbf{k}_{\parallel} . The proof of this first property is given by Kreigher [8] by observing that the characteristic polynomial P resulting from equation (11) is of the form,

$$P = E^N + \gamma_1(\mathbf{k})E^{N-1} + \gamma_2(\mathbf{k})E^{N-2} + \dots + \gamma_{N-1}(\mathbf{k})E + \gamma_N(\mathbf{k}) = 0. \quad (12)$$

Since the matrix elements of $\bar{\bar{H}}(\mathbf{k})$ are polynomial functions of \mathbf{k} , then the coefficients $\gamma_i(\mathbf{k})$ ’s in (12) are also polynomials in the components of \mathbf{k} . It is important here to recall the definition of a polynomial: it is an expression consisting of variables and coefficients, that involves only the operations of addition, subtraction, multiplication, and non-negative integer exponents of variables. No division is allowed in the definition, a fact that will be important later. Since the $E_i(\mathbf{k})$ are solutions of an algebraic equation, whose coefficients are polynomials of \mathbf{k} , and a polynomial function is analytic at every point in \mathbb{C} , one can conclude that the $E_i(\mathbf{k})$ are analytic functions for each \mathbf{k} , except at a set of singular points, where two $E_i(\mathbf{k})$ connects, namely the branch points of $E(\mathbf{k})$. Kreigher [8] also showed that these branch point must exist, but this is less important for our theory. The take-home message at this point is that there are no singularities other than the branch points.

- (b) E is real for real \mathbf{k} and, in general, $E(\mathbf{k}) = E^*(\mathbf{k}^*)$, where the symbol $*$ indicates the complex conjugate. The proof of the first statement is straightforward, since for real \mathbf{k} the matrix $\bar{\bar{H}}(\mathbf{k})$ is Hermitian, hence its eigenvalues $E_i(\mathbf{k})$ must be real. Moreover, the characteristic polynomial (12) can be written as,

$$P = [E - E_1(\mathbf{k})][E - E_2(\mathbf{k})] \dots [E - E_N(\mathbf{k})] = 0. \quad (13)$$

Hence the coefficients $\gamma_i(\mathbf{k})$ are the sum of products of the $E_i(\mathbf{k})$'s, which are real for real \mathbf{k} . This is sufficient to conclude that for any \mathbf{k} , $\gamma_i^*(\mathbf{k}) = \gamma_i(\mathbf{k}^*)$. By applying the latter equality on the complex conjugate of (12), we finally have $E(\mathbf{k}) = E^*(\mathbf{k}^*)$.

- (c) Along the component of the wave vector allowed to be complex, k , in the neighborhood of a branch point, $k = q$, the energy behaves as

$$E(k) = E(q) + \alpha(k - q)^{1/2}, \quad (14)$$

where α is a constant (in general $q = q(\mathbf{k}_{\parallel})$). The proof of this statement is rooted in interpreting the polynomial (12) as a function of E and k , expanded as a Taylor series in two variables around $k = q$ and $E = E(q)$, namely

$$\begin{aligned} P(E, k) &= P(E(q), q) \\ &+ (E - E(q)) \left. \frac{\partial P}{\partial E} \right|_{\substack{k=q \\ E=E(q)}} + (k - q) \left. \frac{\partial P}{\partial k} \right|_{\substack{k=q \\ E=E(q)}} \\ &+ \frac{1}{2} (E - E(q))^2 \left. \frac{\partial^2 P}{\partial E^2} \right|_{\substack{k=q \\ E=E(q)}} + \dots \end{aligned} \quad (15)$$

By looking at equation (13), $P(E(q), q)$ is zero and so is the first derivative with respect to the energy evaluated at $E(q)$. In fact q is the branch point, where two $E_i(\mathbf{k})$ surfaces are equal. This means that (13) is proportional to $(E - E(q))^2$, whose derivative is zero for $E = E(q)$. In conclusion, in first approximation one has

$$\begin{aligned} P(E, k) &= (k - q) \left. \frac{\partial P}{\partial k} \right|_{\substack{k=q \\ E=E(q)}} \\ &+ \frac{1}{2} (E - E(q))^2 \left. \frac{\partial^2 P}{\partial E^2} \right|_{\substack{k=q \\ E=E(q)}} = 0, \end{aligned} \quad (16)$$

leading directly to (14).

- (d) Branch points come always in pairs. In fact, if q is a branch point, also q^* is. This derives directly from point (b).
- (e) The branch points occur always at a complex k . The statement is consequence of the fact that when two bands meet at a real q , this is no longer a branch point of $E(k)$. Take q approaching the real axis, then also q^* does approach it. Hence, the energy can be expanded as,

$$E(k) = E(q) + \alpha(k - q)^{1/2}(k - q^*)^{1/2} \sim (k - q), \quad (17)$$

that is not a branch point.

- (f) $E(\mathbf{k})$ is periodic in k for real k 's and, of course, along the other two components of the wavevector, \mathbf{k}_{\parallel} . One can write,

$$E(\mathbf{k}) = E(\mathbf{k} + \mathbf{G}), \quad (18)$$

where \mathbf{G} is a reciprocal lattice vector, strictly real. This means that the entire CBS follows the periodicity in real k . The proof of this statement is from Heine [4].

So far we focused on the entire complex dispersion relation $E(\mathbf{k})$ (including complex energy values). The next statements

concern instead the ‘lines of real energy’, namely the lines forming the CBS of a material. These are the allowed energies with $\Im(E(\mathbf{k})) = 0$ (see figure 2). In this list we focus on the k component only, with \mathbf{k}_{\parallel} being treated just as a parameter.

- (g) A direct consequence of point (b) is that $E(\Re(k) + i\Im(k)) = E(\Re(k) - i\Im(k))$. This means that, if k returns real energies, also its complex conjugate will. Although not plotted explicitly in figure 2, all bands have a mirror symmetric at $-\Im(k)$.
- (h) The real bands (energies associated to k 's with $\Im(k) = 0$) are, of course, part of the lines of real energy. However, these have additional properties when going in the complex plane. At every maximum or minimum in a real band, the energy makes a 90° turn to go into an imaginary plane (a plane where $\Re(k)$ is constant). More precisely, a maximum or a minimum of the real bands is a point where four real energies meet: the two in the real plane coming from the left and the right of the maximum/minimum, and two in the imaginary plane, one going toward positive $\Im(k)$ and one going toward negative $\Im(k)$. Both these branches are necessarily present due to point (g). Moreover, a minimum in the real bands correspond to a maximum in the imaginary plane and vice-versa a maximum in the real bands correspond to a minimum in the imaginary plane. Therefore the point where the four real energies meet is a saddle point for the full dispersion relation $E(k)$. The proof of this statement follows from a simple expansion of $E(k)$ around any point in the real plane, k_0 ,

$$\begin{aligned} E(k) &= E(k_0) + (k - k_0) \left. \frac{\partial E}{\partial k} \right|_{k=k_0} \\ &+ \frac{1}{2} (k - k_0)^2 \left. \frac{\partial^2 E}{\partial k^2} \right|_{k=k_0} + \dots \end{aligned} \quad (19)$$

For k just outside the real plane, the first derivative must be real to have real $E(k)$, otherwise $(k - k_0)$ would bring an imaginary contribution. Therefore, only at maxima or minima one can have real energies coming from complex k 's. By analyzing now the second order term, we find that $(k - k_0)^2$ will be real only if k is real or if $\Re(k) = k_0$. In our example of figure 2 we can observe the behavior just described. In fact, a complex band leaves the $\Im(k) = 0$ plane every time a pure real band has a maximum of a minimum, including wave vectors at the Brillouin zone boundaries. There is no guarantee that the line remains in the imaginary plane at every energy. In other words it is possible to have a line of real energy, where the real and imaginary parts of k change simultaneously.

- (i) Lines of real energy that leave the real plane, return to the real plane after going around one or more branch points. The line does not necessarily go into a branch point, but this happens, for example, when there is a mirror plane between the layers of the layered structure [4, 10]. A proof of this statement is not presented here, but we observe that the argument holds for both finite models and general Hamiltonians. This explains the semicircular-shaped bands seen in figure 2, the so-called type-1 bands.

(j) The other behavior of the lines of real energy described in literature is when a line goes toward $E = -\infty$, while $\Im m(k)$ goes to $\pm\infty$. This feature is not mentioned by Kreigher [8], however it is analyzed extensively by Heine for the full Hamiltonian [4]. For strictly 1D system, just two of such lines are present. However in 3D, an infinite set of such bands is expected. These are the type-2 lines of figure 2.

(k) Heine proved that the lines of real energy do not split, begin or terminate [4]. Moreover, their chance of crossing is vanishing small except for energies on the real plane.

In concluding this section, let us summarize the general picture. The full dispersion relation is a multi-valued function in the complex plane formed by Riemann surfaces connected by branch points. The lines of real energy, forming the CBS of a material, are expected to have a peculiar behavior: starting from $E = -\infty$, one can follow a line of real energy winding up to larger energies and jumping on and off the real plane in a continuous way. The line leaves the real axis when there is a maximum or a minimum, and it comes back to it after going around a branch point. We remark here that, although the analytical properties just presented naturally explains both type-1 and type-2 bands, they do not cover the behavior of the type-3 ones.

4. Few more insights into finite-band models

All the properties discussed in the previous section are valid in general and for finite-band models [8]. The only exceptions are (f), (j) and (k), which deserve further discussion. Point (f) concerns real bands and it is less relevant for our discussion.

Statement (j) establishes the existence of type-2 bands for $E \rightarrow -\infty$, when $\Im m(k) \rightarrow \pm\infty$. Our numerical results suggest that in the case of finite-band models the statement needs to be broadened to the case of bands running to $E = +\infty$. In fact, the spectrum of a generic periodic Hamiltonian is not upper bounded, namely the number of real bands is infinite. This means that any line of real energy can return to the real plane to form a type-1 band. In contrast, in finite-band models the spectrum can be bounded both from below and from above, opening the possibility of a type-2 band for $E \rightarrow +\infty$. This argument is demonstrated in figure 5, where we present the bands of MgS along [111] at $\mathbf{k}_{\parallel} = (0, 0)$. The results in the (upper panel) are for a minimal basis set containing only a single Mg 3s orbital, one S 2s and the triple-degenerate S 2p's. One can clearly notice two complex bands diverging at positive energies. The first one originates just below the Fermi level (red band) and goes rapidly toward high energies. The second one starts at about 10 eV above E_F (blue band) and has a much slower rate of increase. This second band can be transformed into a type-1 by adding to the basis set an additional orbital of s symmetry, as shown in the (lower panel) of figure 5. The inclusion of an additional s orbital generates a new high-energy real band (starting at about 23 eV above E_F), which offers a point on the real axis where to close its imaginary counterpart. In doing so the type-2 band is transformed in a type-1 going from 10 eV to about 23 eV. Note, however,

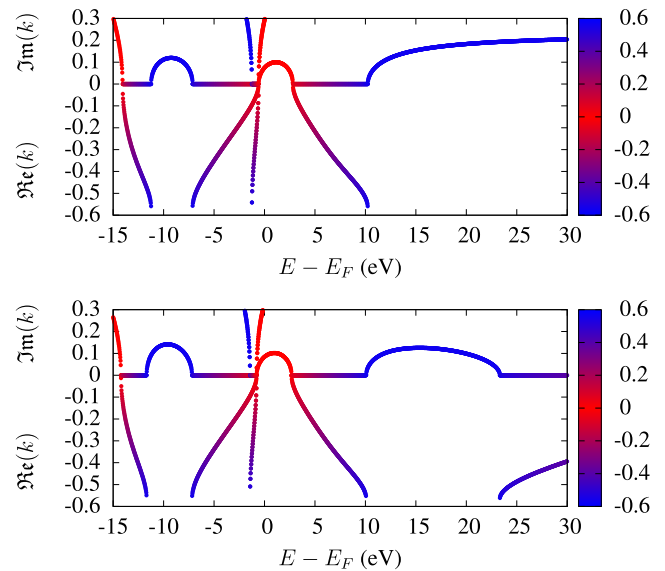


Figure 5. CBS for MgS along the [111] direction at $\mathbf{k}_{\parallel} = (0, 0)$. The (upper panel) displays calculations performed with a minimal basis set containing 5 orbitals (Mg s , S s , S p), while an additional s orbital is included in the results shown in the (lower panel). The vertical axis is divided into two regions. Pure real bands ($\Re e(k)$), obtained when $\Im m(k) = 0$ are reported below the origin (this is the standard band structure). Imaginary bands are shown above the origin. The colors encode the real component of the wave-vector, $\Re e(k)$ (pure imaginary bands have $\Re e(k) = 0$). The units of k are 1/Bohr.

that a new type-2 band (not shown on the scale of figure 5) is then created at the second band edge of the new high-energy real one. Note also that the addition of the new orbital does not affect the runaway complex band starting just below the Fermi level. This is because the associated real one is doubly degenerate with O p_x-p_y character (the orbital directions are taken here with respect to the MgS [111] crystal direction), and no new orbitals with p (or p -compatible) symmetry have been added to the basis set. Demonstration of the fact that the newly added orbital is of s nature is reported in appendix A, where the partial density of states of the two calculations is displayed.

Finally, concerning point (k), Heine's proof [4] based on the concept of winding number is not easily extensible outside complex analysis. In practice, in our calculation we find that the situations of splitting and merging bands is very rare, but it is encountered. Similar results were reported before [23] for CBS constructed with orthogonal basis sets. Therefore, we conclude that the property (j) is probably not valid when the band structure is finite.

5. The case of non-orthogonal basis sets

In this section we discuss the origin of the type-3 complex bands, which have been observed several times before but never investigated in detail. To the best of our knowledge these do not appear in any review of the analytic properties of the CBS. We start by considering a simple model describing a 1D chain containing alternating atoms of different type with lattice constant $a = 1$ (see figure 6). Let us consider non-interacting electrons.

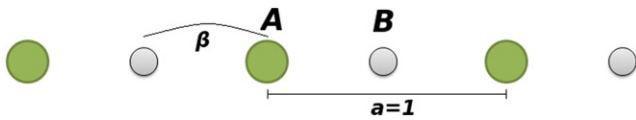


Figure 6. Diatomic 1D chain model used for the calculation of the CBS. The system is described by a tight-model with on-site energies ε_A and ε_B and a single hopping integral β . The lattice constant is $a = 1$.

The problem is treated at the level of first nearest-neighbors tight-binding model with a single hopping parameter β and two different on-site energies, respectively, ε_A and ε_B . The tight-binding Bloch wave function writes

$$\varphi(r) = \sum_j e^{ikj} [c_A \phi_{Aj}(r) + c_B \phi_{Bj}(r)], \quad (20)$$

where $\phi_{\alpha j}(r)$ is the atomic orbital of type α ($\alpha = A$ and B) in the j th cell and the c_α 's are coefficients. For the moment let us assume the $\phi_{\alpha j}(r)$ orbitals to be orthonormal. The secular equation of the model simply reads

$$\begin{bmatrix} \varepsilon_A & \beta(1 + e^{-ik}) \\ \beta(1 + e^{ik}) & \varepsilon_B \end{bmatrix} \begin{bmatrix} c_A \\ c_B \end{bmatrix} = E(k) \begin{bmatrix} c_A \\ c_B \end{bmatrix}, \quad (21)$$

and has solution

$$E(k) = \Sigma \pm \sqrt{\Xi^2 + 2\beta^2[1 + \cos(k)]}, \quad (22)$$

where we have defined

$$\Sigma = \frac{\varepsilon_A + \varepsilon_B}{2}, \quad \Xi = \frac{\varepsilon_A - \varepsilon_B}{2}. \quad (23)$$

Thus, we have two real bands separated by a bandgap at the edge of the Brillouin zone proportional to Ξ .

Let us now extend equation (22) to the complex k plane. One can write $\cos(k)$ as a complex quantity

$$\cos(k) = \frac{e^{i\Re(k) - \Im(k)} + e^{-i\Re(k) + \Im(k)}}{2}, \quad (24)$$

which is clearly real for $\Im(k) = 0$, but also when $\Re(k) = n\pi$ with $n = 0, \pm 1, \pm 2, \dots$. One can then distinguish two cases, namely

- n even (or $n = 0$)

$$\cos(k) = \frac{e^{\Im(k)} + e^{-\Im(k)}}{2} = \cosh[\Im(k)], \quad (25)$$

- n odd

$$\cos(k) = \frac{-e^{\Im(k)} - e^{-\Im(k)}}{2} = -\cosh[\Im(k)]. \quad (26)$$

We can then plot the lines of real energy, which are displayed in figure 7 for $\varepsilon_A = 7$, $\varepsilon_B = 3$ and $\beta = 2.3$. Because of the simplicity of the model, a conventional representation where E is on the vertical axis, while the wave vector is on the horizontal one, is adequate. The picture is divided into three panels: in the (middle) we plot the energy for real k (the standard band structure), the (left-hand side panel) shows

the allowed energies as a function of $\Im(k)$ when $\Re(k) = 0$ (pure imaginary bands), while the (right-hand side) one is for $\Re(k) = \pi$. In order to allow a comparison with the complex bands computed with SIESTA and presented in the previous section we also re-plot the same bands as an E -vs- k diagram, where now the real component of the wave-vector is displayed through a color map. All the properties discussed before for the lines of real energy, are respected by the model. The line comes from $E = -\infty$ with pure imaginary k and joins the real plane at $\Re(k) = 0$, forming the first real band. At $\Re(k) = \pi$ it makes another 90° rotation in the imaginary plane, it reaches a maximum and then it comes back toward $k = \pi + i0^+$ to join to the second real band. The finite nature of the model makes impossible for the line to stay on the real plane, while $E \rightarrow \infty$. This gives a pure imaginary band ($\Re(k) = 0$, (left-hand side panel) of figure 7) that goes to $+\infty$. A mirror image of the (central panel) describes the bands between $\Re(k) = -\pi$ and $\Re(k) = 0$ (not depicted), and the negative values of $\Im(k)$ have the same energy of the corresponding positive values. Therefore, we have two lines of real energy, as expected for pure 1D situations [4].

Let us now relax the orthogonality condition and assume that the basis orbitals on adjacent sites have non-vanishing inner product, S . The secular equation (21) now becomes

$$\begin{bmatrix} \varepsilon_A & \beta(1 + e^{-ik}) \\ \beta(1 + e^{ik}) & \varepsilon_B \end{bmatrix} \begin{bmatrix} c_A \\ c_B \end{bmatrix} = E(k) \begin{bmatrix} c_A \\ c_B \end{bmatrix}, \quad (27)$$

leading to the energies

$$E(k) = \frac{\Sigma - 2\beta S[1 + \cos(k)]}{1 - 2S^2[1 + \cos(k)]} \pm \sqrt{\frac{\Xi^2 + 2[1 + \cos(k)](\beta - S\varepsilon_A)(\beta - S\varepsilon_B)}{[1 - 2S^2(1 + \cos(k))]^2}}. \quad (28)$$

It is now possible to write $\cos(k)$ as a function of the energy and, by taking the inverse, to obtain an analytic expression for $k(E)$

$$k(E) = \arccos \left[\frac{(\varepsilon_A - E)(\varepsilon_B - E)}{2(\beta - ES)^2} - 1 \right], \quad (29)$$

Finally, equation (29) is inverted numerically to find the (left-hand side and the right-hand side panels) of figure 8.

The first clear difference between the orthogonal and non-orthogonal cases is the presence of a divergence (a pole) in the line of real energy displayed on the (left-hand side panel) of figure 8. This happens at $k = \arccos(-1 + 1/2S^2)$. If the overlap parameter is $S > 1/2$, the divergence will appear at a real k . Such condition, however, is never met, since the overlap matrix must be positive definite. In fact, the overlap matrix is Hermitian for real k and, therefore, it will be positive definite only if the eigenvalues are positive. These can be calculated to be

$$\lambda_{S,\pm} = 1 \pm \sqrt{2S^2[1 + \cos(k)]}. \quad (30)$$

One then notices that $\lambda_{S,+}$ is always positive, but $1 - \sqrt{2S^2[1 + \cos(k)]}$ is positive for every k only when $S < 1/2$.

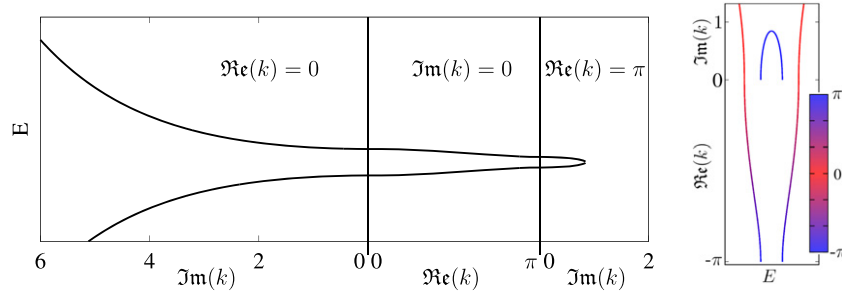


Figure 7. Real (middle panel of the black-and-white figure) and complex (right and left panels of the black-and-white figure) bands for the two sites, nearest-neighbor, tight-binding model with choice of parameters $\varepsilon_A = 7$, $\varepsilon_B = 3$, $\beta = 2.3$. In the (left panel) of the black-and-white figure $\Re k = 0$, thus it reports pure imaginary bands, while in the (right panel) $\Re k = \pi$. The colored figure presents the same bands, now according to the convention used for other CBSs throughout the paper. Pure real bands ($\Im k = 0$) are reported below the origin (this is the standard band structure). Imaginary bands are shown above the origin. The colors encode the real component of the wave-vector, $\Re k$ (pure imaginary bands have $\Re k = 0$).

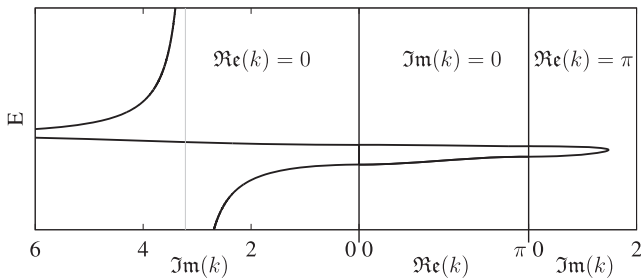


Figure 8. Same bands as in figure 7 but now computed for a non-orthogonal basis with overlap parameter $S = 0.2$. The gray line indicates the position of the pole in $E(k)$.

Hence, the fact that the overlap matrix is positive definite, prevents the divergence to be in the real bands, but this may still appear for complex k 's.

The presence of a divergence brings a major concern, since it is in contrast with the analytical property (a) of $E(\mathbf{k})$ (see section 3). In fact, it is not true that the dispersion relation is analytic for each point in k -space except the branch points. There is the possibility of a singularity that is a pole. Looking back at the derivation from Kreigher [8], we have found that an important issue has not been stressed. In equation (12) $E_i(\mathbf{k})$ are analytic because the $\gamma_i(\mathbf{k})$'s coefficient are polynomial functions, but also because the leading term, E^N , is one. This is an essential condition. If it is relaxed, the $E_i(\mathbf{k})$ might only be identified as meromorphic functions. An easy example is sufficient to prove this statement. Take two polynomial functions $a(k)$ and $b(k)$; a relation of the type $a(k) = \varepsilon b(k)$ leads to a $\varepsilon(k)$ with a pole at q anytime $b(k)$ has a zero at q .

The Schrödinger equation (11) in the case of non-orthogonal basis set becomes a generalized eigenvalue problem

$$\bar{H}(\mathbf{k})\mathbf{c} = E\bar{S}(\mathbf{k})\mathbf{c}. \quad (31)$$

The characteristic polynomial is now the determinant of $(\bar{H} - E\bar{S})$, which leads to an equation similar to (12), where the coefficient of the leading power is not one. If this coefficient depends on \mathbf{k} and has a zero, then $E_i(\mathbf{k})$ may have a pole. Alternatively, one could invert the overlap matrix to return to a standard eigenvalue problem. In our model the Schrödinger

equation will become

$$\frac{1}{N(k)} \begin{bmatrix} \varepsilon_A - 2\beta S[1 + \cos(k)] & (\beta - S\varepsilon_B)[1 + e^{-ik}] \\ (\beta - S\varepsilon_A)(1 + e^{ik}) & \varepsilon_B - 2\beta S[1 + \cos(k)] \end{bmatrix} \begin{bmatrix} c_A \\ c_B \end{bmatrix} = E(k) \begin{bmatrix} c_A \\ c_B \end{bmatrix}, \quad (32)$$

with $N(k) = 1 - 2S^2[1 + \cos(k)]$. Now, the matrix elements are not polynomials because of the denominator, $N(k)$, so that the pole is still present.

We have then proved that the presence of a pole in the dispersion relation, $E(\mathbf{k})$, is admissible when a non-orthogonal basis set is employed. This gives rise to the flat (when $k(E)$ is plotted) complex bands, here termed type-3, and observed in the past. In fact the pole value is an asymptote (gray line in figure 8) that the complex bands approach and never reach, giving origin to the flat behavior. This singularity cannot affect the real bands, since the overlap matrix is positive definite. However, it can be seen for complex values of \mathbf{k} .

6. Discussion and conclusion

In conclusion we have implemented the transfer matrix technique to compute the complex bands of electronic structures obtained from density functional theory. The method is implemented in the DFT package SIESTA and allows one to calculate the complex bands along an arbitrary crystalline direction and particular transverse k point. The method is conceived as a post-processing tool and therefore it is amenable to be used for high-throughput studies.

Three types of complex bands are identified depending on their behavior on the complex plane. Type-1 bands have a semicircular shape with their edges connected at real-band band-edges on the real axis. These are the most frequently founded in literature. In contrast type-2 bands originate also at a band edge on the real axis but then they diverge. The divergence to $E \rightarrow -\infty$ is a direct consequence of the fact that the spectrum is bounded from below, while the one to $E \rightarrow +\infty$ is found only for finite-band models (as in our case), where the spectrum is also bounded from above. Type-1 and type-2

bands are expected from the known analytic properties of the band structure, which we have here reviewed.

When computing the complex bands with SIESTA a third type appears. These bands do not originate from a point on the real axis and they run flat at a constant energy. Bands of these types have been reported in the past in numerical exercises, but their origin has never been discussed. In fact, their features appear to lie outside the analytic properties of the band structure. Our numerical investigation proves that those bands are the result of the non-orthogonality of the basis set, which creates poles in the CBS. A simple analysis, conducted over a model 1D structure, reveals that the actual position of such poles depends solely on the overlap matrix elements, so that the bands have to be considered an artifact of the basis set choice. Crucially, their presence does not affect the curvature of the remaining type-1 and type-2 complex bands and of the conventional real ones. Thus, if one is interested just in understanding the CBS of a material, type-3 bands can simply be neglected.

The problem, however, will be much more severe if the complex bands enter in calculations determining other materials properties. Electron transport in tunnel junctions is a clear example of this situation. In the tunneling regime the decay of the wave function across the tunnel barrier is determined by the CBS of the insulator. For most insulators the relevant complex band is a type-1 connecting the band edges across the gap (these may vary depending on the relative \mathbf{k}_{\parallel}) [6]. If a spurious type-3 band is present due to the non-orthogonality of the basis and this is associated to $\Im m(k)$ values smaller than those of the genuine type-1 band, then the tunneling rates will be determined by such type-3 band, clearly an unphysical situation. The standard practice in those cases is to fine-tune the basis set, for instance by changing the cutoff radii, so to push the spurious type-3 bands well above the genuine type-1 ones [24, 25]. This solution, although practical, is not ideal, since the convergence of the DFT calculations itself becomes constrained by the need of keeping the cutoff radii short so to minimize the non-orthogonality.

A more elegant solution would be that of performing basis orthogonalization. This is not expected to affect the real part of the band structure, but may remove the type-3 complex band. We have investigated in great detail this possibility in appendix B for the simple 1D model. Indeed basis orthogonalization eliminates the type-3 band and transform it into a type-2, but unfortunately the actual curvature of this new type-2 band seems to converge in a somewhat non-trivial way with the truncation done to approximate the orthogonalization matrix. Thus, probably the most effective strategy to eliminate spurious type-3 bands still remain that of fine-tune the original basis set, perhaps by compromising the cutoff of the radial component of the basis function with the number of zetas.

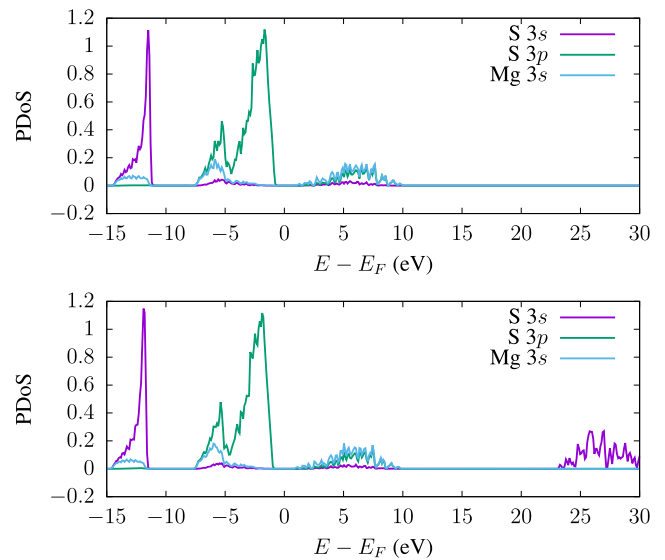


Figure A1. Partial density of states (PDoS) for MgS. The (upper panel) displays calculations performed with a minimal basis set containing 5 orbitals (Mg s , S s , S p), while an additional s orbital is included in the results shown in the (lower panel). The added orbital shows s nature.

Acknowledgments

This work has been supported by the Science Foundation Ireland Principal Investigator award (Grant No. 14/IA/2624 and Amber Center Grant No. 12/RC/2278) and TCHPC (Research IT, Trinity College Dublin). The authors wish to acknowledge the DJEI/DES/SFI/HEA Irish Centre for High-End Computing (ICHEC) for the provision of computational facilities and support.

Data availability statement

The data that support the findings of this study are available upon reasonable request from the authors.

Appendix A. MgS partial density of states

In this appendix we report the partial density of states (PDoS) for the calculations reported in figure 5. The (upper and lower panels) of figure A1 refer to the (upper and lower panels) of figure 5 respectively. It is evident that the band added in the calculation reported in the (lower panel) has an s nature. In particular it can be assigned to the $3s$ orbital of S.

Appendix B. Orthogonalization

In this appendix we discuss how basis set orthonormalization can act on removing the poles of the CBS (type-3 bands). This is applied specifically to the two-band model introduced in section 5. In particular we use the symmetric Löwdin orthogonalization process. Consider the generic wave function,

$$\varphi(r) = \sum_j^{\infty} c_j \phi_j(r), \quad (\text{B.1})$$

where now the index j runs on both the A and B sites. Let us denote with ϕ the vector (infinite) containing all the basis functions, ϕ_j 's. An orthogonal basis ϕ' is then obtained by applying the following linear transformation

$$\phi' = \bar{S}^{-1/2} \phi, \quad (\text{B.2})$$

where \bar{S} is the overlap matrix. Note that the orthogonalization process concerns the entire basis so that \bar{S} is an infinite matrix. Assuming, as before, that the non-vanishing overlap matrix elements concern only nearest-neighbour orbitals, this reads

$$\bar{S} = \begin{bmatrix} \dots & \dots & \dots & \dots & \dots & \dots & \dots \\ \dots & 1 & S & 0 & 0 & 0 & \dots \\ \dots & S & 1 & S & 0 & 0 & \dots \\ \dots & 0 & S & 1 & S & 0 & \dots \\ \dots & 0 & 0 & S & 1 & S & \dots \\ \dots & 0 & 0 & 0 & S & 1 & \dots \\ \dots & \dots & \dots & \dots & \dots & \dots & \dots \end{bmatrix}. \quad (\text{B.3})$$

Given \bar{S} , the matrix $\bar{S}^{-1/2}$ can be obtained numerically with a number of techniques. Here we will investigate two options. The first one is Schur's algorithm [26], which approximates the infinite $\bar{S}^{-1/2}$ matrix with large finite ones, while the second consists in constructing a Taylor expansion for $\bar{S}^{-1/2}$. In this case one writes \bar{S} as

$$\bar{S} = 1 + \Delta\bar{S}, \quad (\text{B.4})$$

where 1 is the infinite identity matrix and $\Delta\bar{S} = \bar{S} - 1$. The Taylor expansion of $\bar{S}^{-1/2}$ is then constructed around $\bar{S} = 1$ ($\Delta\bar{S} \rightarrow 0$)

$$\bar{S}^{-1/2} = (1 + \Delta\bar{S})^{-1/2} = 1 - \frac{1}{2}\Delta\bar{S} + \frac{3}{8}\Delta\bar{S}^2 - \frac{5}{16}\Delta\bar{S}^3 + \dots \quad (\text{B.5})$$

the approximation then consists in where to truncate the expansion. The benefits of this second approach are that there is a simple analytic expression for the power of $\Delta\bar{S}$ (see appendix C) and that, at least at the lower orders, one can write an analytic expression for the dispersion relation. In what follows we will show results for both Schur's algorithm and truncated Taylor expansions. Once $\bar{S}^{-1/2}$ has been computed the matrix Schrödinger equation will simply write

$$\bar{S}^{-1/2} \bar{H} \bar{S}^{-1/2} \mathbf{c} = E \mathbf{c}, \quad (\text{B.6})$$

where \bar{H} is the infinite matrix representing the Hamiltonian over the non-orthogonal basis,

$$\bar{H} = \begin{bmatrix} \dots & \dots & \dots & \dots & \dots & \dots & \dots \\ \dots & \varepsilon_A & \beta & 0 & 0 & 0 & \dots \\ \dots & \beta & \varepsilon_B & \beta & 0 & 0 & \dots \\ \dots & 0 & \beta & \varepsilon_A & \beta & 0 & \dots \\ \dots & 0 & 0 & \beta & \varepsilon_B & \beta & \dots \\ \dots & 0 & 0 & 0 & \beta & \varepsilon_A & \dots \\ \dots & \dots & \dots & \dots & \dots & \dots & \dots \end{bmatrix}. \quad (\text{B.7})$$

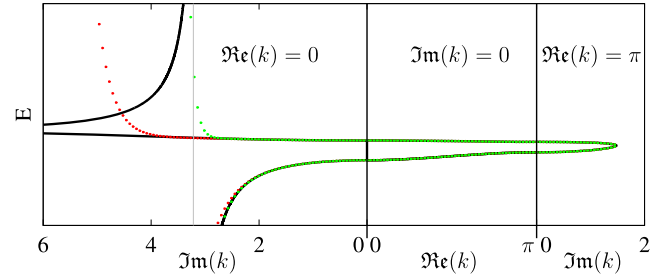


Figure B1. Real (middle panel) and complex (right and left panels) bands for the two sites, nearest-neighbor, tight-binding model constructed over a non-orthogonal basis set. The model parameters are $\varepsilon_A = 7$, $\varepsilon_B = 3$, $\beta = 2.3$ and $S = 0.2$. In the (left-hand side panel) $\Re(k) = 0$ (pure imaginary bands). In the (right-hand side panel) $\Re(k) = \pi$. The black line is for the non-orthogonal model, while the colored dots are the bands obtained after Schur's orthonormalization procedure, where the $\bar{S}^{-1/2}$ is approximated with either a 20×20 (red dots) or a 50×50 matrix (green dots).

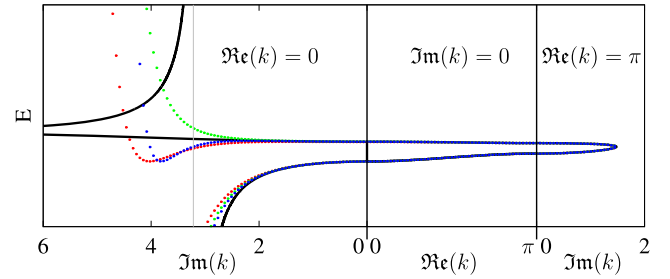


Figure B2. Real (middle panel) and complex (right and left panels) bands for the two sites, nearest-neighbor, tight-binding model constructed over a non-orthogonal basis set. The model parameters are $\varepsilon_A = 7$, $\varepsilon_B = 3$, $\beta = 2.3$ and $S = 0.2$. In the (left-hand side panel) $\Re(k) = 0$ (pure imaginary bands). In the (right-hand side panel) $\Re(k) = \pi$. The black line is for the non-orthogonal model, while the colored dots are the bands obtained after orthonormalization using a Taylor expansion of $\bar{S}^{-1/2}$: red = third order, green = fourth order and blue = fifth order.

At this point Bloch's theorem can be applied to obtain the final band structure.

Our numerical results for the Schur's algorithm are presented in figure B1, while those obtained through the Taylor expansion are in figure B2.

Let us first consider figure B1. Clearly the orthonormalization process leaves unchanged both the real and the complex semicircular (type-1) bands. In contrast, the CBS at $\Re(k) = 0$ is drastically modified by the orthogonalization. The complex band going to a finite wave vector for $E \rightarrow -\infty$ is similar to the non-orthogonal case, however, in the approximation that we consider, this band does not present the same asymptote of the non-orthogonal case. It is not clear whether this is just an approximation effect or it would stand also for the exact solution. In fact, increasing the precision we can see the band flattening out and resembling more and more the asymptotic behavior of the non-orthogonal case. A similar discussion can be done for the second branch at $\Re(k) = 0$ (the one going to $E \rightarrow +\infty$). The band appears to remain relatively flat at any

level of approximation and to approach an asymptotic behavior when increasing the precision of the numerical calculation. For this branch, however, the asymptote would be reached from below and not from above, a feature that distinguishes the orthogonal from the non-orthogonal case. We conclude that the orthogonalization procedure with the Schur's algorithm [26], which approximates the infinite $\bar{S}^{-1/2}$ matrix with large finite ones, transforms the type-3 bands of the non-orthogonal case in type-2 bands with heavy curvature. However it is not possible to conclude whether this effect is due to the approximations taken or it is maintained for an exact orthogonalization.

It is also interesting to see how the Taylor expansion approach works, figure B2. Also in this case the real bands are well described and they become indistinguishable from those computed with the non-orthogonal model as the order of the Taylor expansion grows. A very similar feature is found for the type-1 complex band, which in fact converges already at low order. The behavior of the $\Re(k) = 0$ part of the complex bands is somehow different. On the one hand, the $E \rightarrow -\infty$ branch appears to slowly converge to the non-orthogonal band as the order of the Taylor expansion gets higher. This is similar to what we found for the Schur's orthonormalization procedure. On the other hand, the $E \rightarrow +\infty$ branch turns from type-3 to type-2-like, although the change in the actual shape of the band depends on the level of approximation in a non-trivial way. Once again it is not clear whether or not an asymptotic behavior would appear for the full expansion.

In conclusion, our numerical analysis has shown that standard orthogonalization can be used to remove the poles of the CBS originating from the non-orthogonality of the basis set (type-3 bands). The two techniques shown here reproduce well both the real bands and the complex type-1 ones, even at a rather low level of approximation. Furthermore, type-3 bands are transformed in type-2 ones. However, such new type-2 bands appear to have an heavy curvature that makes them almost flat, lessening the utility of the orthogonalization in practical cases.

Appendix C. Power expansion of $\Delta\bar{S}$

We report here the analytic expression of the powers of $\Delta\bar{S}$ used in appendix B

$$\Delta\bar{S} = \begin{bmatrix} \dots & \dots & \dots & \dots & \dots & \dots & \dots \\ \dots & 0 & S & 0 & 0 & 0 & \dots \\ \dots & S & 0 & S & 0 & 0 & \dots \\ \dots & 0 & S & 0 & S & 0 & \dots \\ \dots & 0 & 0 & S & 0 & S & \dots \\ \dots & 0 & 0 & 0 & S & 0 & \dots \\ \dots & \dots & \dots & \dots & \dots & \dots & \dots \end{bmatrix}. \quad (\text{C.1})$$

$$\Delta\bar{S}^2 = \begin{bmatrix} \dots & \dots & \dots & \dots & \dots & \dots & \dots \\ \dots & 2S^2 & 0 & S^2 & 0 & 0 & \dots \\ \dots & 0 & 2S^2 & 0 & S^2 & 0 & \dots \\ \dots & S^2 & 0 & 2S^2 & 0 & S^2 & \dots \\ \dots & 0 & S^2 & 0 & 2S^2 & 0 & \dots \\ \dots & 0 & 0 & S^2 & 0 & 2S^2 & \dots \\ \dots & \dots & \dots & \dots & \dots & \dots & \dots \end{bmatrix}. \quad (\text{C.2})$$

$$\Delta\bar{S}^3 = \begin{bmatrix} \dots & \dots & \dots & \dots & \dots & \dots & \dots \\ \dots & 0 & 3S^3 & 0 & S^3 & 0 & \dots \\ \dots & 3S^3 & 0 & 3S^3 & 0 & S^3 & \dots \\ \dots & 0 & 3S^3 & 0 & 3S^3 & 0 & \dots \\ \dots & S^3 & 0 & 3S^3 & 0 & 3S^3 & \dots \\ \dots & 0 & S^3 & 0 & 3S^3 & 0 & \dots \\ \dots & \dots & \dots & \dots & \dots & \dots & \dots \end{bmatrix}. \quad (\text{C.3})$$

$$\Delta\bar{S}^4 = \begin{bmatrix} \dots & \dots & \dots & \dots & \dots & \dots & \dots \\ \dots & 6S^4 & 0 & 4S^4 & 0 & S^4 & \dots \\ \dots & 0 & 6S^4 & 0 & 4S^4 & 0 & \dots \\ \dots & 4S^4 & 0 & 6S^4 & 0 & 4S^4 & \dots \\ \dots & 0 & 4S^4 & 0 & 6S^4 & 0 & \dots \\ \dots & S^4 & 0 & 4S^4 & 0 & 6S^4 & \dots \\ \dots & \dots & \dots & \dots & \dots & \dots & \dots \end{bmatrix}. \quad (\text{C.4})$$

ORCID iDs

E Bosoni  <https://orcid.org/0000-0003-4585-5478>

S Sanvito  <https://orcid.org/0000-0002-0291-715X>

References

- [1] Yablonoivitch E 1987 Inhibited spontaneous emission in solid-state physics and electronics *Phys. Rev. Lett.* **58** 2059
- [2] John S 1987 Strong localization of photons in certain disordered dielectric superlattices *Phys. Rev. Lett.* **58** 2486
- [3] Kohn W 1959 Analytic properties of Bloch waves and Wannier functions *Phys. Rev.* **115** 809
- [4] Heine V 1963 On the general theory of surface states and scattering of electrons in solids *Proc. Phys. Soc.* **81** 300
- [5] Prodan E 2006 Analytic structure of Bloch functions for linear molecular chains *Phys. Rev. B* **73** 035128
- [6] Butler W H, Zhang X-G, Schulthess T C and MacLaren J M 2001 Spin-dependent tunneling conductance of Fe–MgO–Fe sandwiches *Phys. Rev. B* **63** 054416
- [7] Rungger I and Sanvito S 2008 Algorithm for the construction of self-energies for electronic transport calculations based on singularity elimination and singular value decomposition *Phys. Rev. B* **78** 035407
- [8] Krieger J B 1967 Some analytic properties of finite-band models in solids *Phys. Rev.* **156** 776
- [9] Tomfohr J K and Sankey O F 2002 Complex band structure, decay lengths, and Fermi level alignment in simple molecular electronic systems *Phys. Rev. B* **65** 245105
- [10] Reuter M G 2017 A unified perspective of complex band structure: interpretations, formulations, and applications *J. Phys.: Condens. Matter* **29** 053001
- [11] Soler J M, Artacho E, Gale J D, García A, Junquera J, Ordejón P and Sánchez-Portal D 2002 The SIESTA method for *ab initio* order- N materials simulation *J. Phys.: Condens. Matter* **14** 2745
- [12] García A *et al* 2020 SIESTA: recent developments and applications *J. Chem. Phys.* **152** 204108
- [13] Sanvito S, Lambert C J, Jefferson J H and Bratkovsky A M 1999 General Green's function formalism for transport calculations with *spd* Hamiltonians and giant magnetoresistance in Co- and Ni-based magnetic multilayers *Phys. Rev. B* **59** 11936
- [14] Rocha A R, García-Suárez V M, Bailey S, Lambert C, Ferrer J and Sanvito S 2006 Spin and molecular electronics in atomically generated orbital landscapes *Phys. Rev. B* **73** 085414

- [15] Anderson E *et al* 1999 *LAPACK Users' Guide* 3rd edn (Philadelphia, PA: SIAM) LAPACK: Linear Algebra PACKage <http://netlib.org/lapack/>
- [16] Rong Z, Kitchaev D, Canepa P, Huang W and Ceder G 2016 An efficient algorithm for finding the minimum energy path for cation migration in ionic materials *J. Chem. Phys.* **145** 74112
- [17] Larsen A H *et al* 2017 *J. Phys.: Condens. Matter* **29** 273002
- [18] Bosoni E 2021 <https://github.com/bosonie>
- [19] Bergerhoff G, Brown I D 1987 *Crystallographic Databases* ed F H Allen (Hrsg.) *et al* (Chester: International Union of Crystallography) <https://icsd.products.fiz-karlsruhe.de/>
- [20] Smogunov A, Dal Corso A and Tosatti E 2004 Ballistic conductance of magnetic Co and Ni nanowires with ultrasoft pseudopotentials *Phys. Rev. B* **70** 045417
- [21] Giannozzi P *et al* 2009 QUANTUM ESPRESSO: a modular and open-source software project for quantum simulations of materials *J. Phys.: Condens. Matter* **21** 395502
- [22] Needham T 1998 *Visual Complex Analysis (Comparative Pathobiology-Studies in the Postmodern Theory of Education)* (Oxford: Clarendon)
- [23] Zhang Y-C 1982 Complex band structures of zinc-blende materials *Phys. Rev. B* **25** 605
- [24] Toher C, Rungger I and Sanvito S 2009 Simulating STM transport in alkanes from first principles *Phys. Rev. B* **79** 205427
- [25] Cucinotta C S, Rungger I and Sanvito S 2012 First principles study of electron tunneling through ice *J. Phys. Chem. C* **116** 22129
- [26] Deadman E, Higham N J and Ralha R 2013 Blocked Schur algorithms for computing the matrix square root *Applied Parallel and Scientific Computing (Lecture Notes in Computer Science vol 7782)* ed P Manninen and P Öster (Berlin: Springer)